Microseismicity and lithosphere thickness at a nearly-amagmatic oceanic detachment fault system

Jie Chen, Wayne C Crawford, Mathilde Cannat

Microseismicity and lithosphere thickness at a flip-flop detachment fault system of a nearly-amagmatic mid-ocean ridge

Jie Chen, Wayne C. Crawford, Mathilde Cannat

Université Paris Cité, Institut de physique du globe de Paris, CNRS, F-75005 Paris, France

Correspondence author: Jie Chen (chenjie.geo@outlook.com)

Oceanic detachment faults play a central role in accommodating the plate divergence at slow-ultraslow spreading mid-ocean ridges. Successive flip-flop detachment faults in a nearly-amagmatic region of the ultraslow spreading Southwest Indian Ridge (SWIR) at 64°30'E accommodate ~100% of plate divergence, with mostly ultramafic smooth seafloor. Here we present new microseismicity data, recorded by ocean bottom seismometers, showing that the axial brittle lithosphere is on the order of 15 km thick under the nearly-amagmatic smooth seafloor, which is no thicker than under nearby volcanic seafloor or at more magmatic SWIR detachment systems. Our data reveal that microearthquakes with normal focal mechanisms are colocated with seismically-imaged damage zones of the active detachment fault and of antithetic hanging-wall faults, suggesting that both faults accommodate almost all of plate divergence. The level of the hanging-wall seismicity is significantly higher than that documented at more magmatic detachments of slow-ultraslow ridges, which may be a unique feature of nearly-amagmatic flip-flop detachment systems.

The flip-flop detachment fault system discovered at a nearly-amagmatic region of the ultraslow spreading Southwest Indian Ridge (SWIR; full spreading rate of 14 mm/yr) near 64°30'E represents a previously unknown seafloor spreading mode[1–3] (Fig. 1a). In this mode, detachment faults accommodate nearly 100% of plate divergence, continuously cutting into the footwalls of their predecessors, with flipping polarities every 0.6-1.5 Ma[1,2] (Fig. 1). The resulting seafloor morphology is the so-called smooth seafloor[4], with extensive exposure of mantle-derived peridotites, only patches of hummocky basalts[2], and low-temperature carbonate-brucite hydrothermal chimneys[5]. This newly-discovered seafloor spreading mode differs from the "classic" detachment-volcanic and volcanic-volcanic modes at slow spreading ridges and at more magmatically-robust portions of ultraslow spreading ridges, where at least one plate is dominated by abyssal-hill volcanic seafloor[4,6–9] and the detachment fault is characterized by dome-shaped corrugated surface[10–12].

Seismicity provides a means to study magmatic, tectonic, and hydrothermal processes within the lithosphere of mid-ocean ridges[13–19] (MORs) and is an indirect proxy for the thermal regime by constraining the depth to the base of the brittle lithosphere[20,21]. Here, we present a catalog of 307 microearthquakes recorded during two short (8 and 19 days for the SMSMO and RVSMO catalogs, respectively) ocean bottom seismometer (OBS) deployments (Figs. 1 and 2a; Methods). These microearthquakes and 8 focal mechanisms (Methods) reveal a unique distribution of geodynamic stress and accommodation at the youngest active detachment system (DF1) of the SWIR 64°30'E.

Results and discussion

Microseismicity at the SWIR 64°30'E

The two short OBS deployments offer snapshots in time of the seismic activity at the youngest active detachment system. The average seismicity rate is 11.4 events per day (8.4

and 12.7 events per day in the SMSMO and RVSMO catalogs, respectively), including a 34-event seismic swarm in the RVSMO catalog, from Dec 22-23, 2016 (Supplementary Fig. 5). Most microearthquakes occurred in the axial valley (Fig. 2a) between the emergence of DF1 (E1) and the breakaway of DF2 (B2). The highest number of events is recorded near the P2-P2' cross-axis profile (Figs. 2a and 2c). Earthquake hypocenters have depths between 0 and 15 km below the seafloor (bsf), and events in the shorter SMSMO catalog were mostly at less than 10 km bsf (Fig. 2b). Local magnitudes (M_L) range from -0.5 to 3.2, with a magnitude of completeness of 1.1 and a b-value of 0.9 based on the Gutenberg-Richter relation[22] (Methods and Supplementary Fig. 6). Focal mechanisms (Methods) correspond to normal faulting, as expected in an extensional context, except for one strike-slip faulting event (Fig. 2a).

Many microearthquake hypocenters plotted in the cross-axis profiles P1-P1' and P2-P2' (Figs. 2d and 2e) are aligned with the trace of the subseafloor detachment fault plane as inferred from a series of subparallel seismic reflectors with a dip of 50-60°[23,24]. In all three cross-axis profiles, and particularly P3-P3', several events are scattered in the detachment hanging wall. Focal mechanisms of these hanging-wall earthquakes display a prevalence of normal faults with an average dip of 50° at 2-7 km bsf (Figs. 2e and 2f). These dips are consistent with the geometry of nearby north-dipping seismic reflectors[23] (Fig. 2f) and with small-offset fault scarps at the seafloor[2], suggesting that these small faults are conjugate with the detachment fault.

Along the ridge axis (P0-P0'), we also observed a larger number of earthquakes at the transition between volcanic and smooth seafloor (near the P2-P2' profile; Figs. 2c and 2e). Combining this observation with the previous observation of subhorizontal seismic reflectors interpreted as intrusive magmatic sills beneath this transition[24], we propose that seismicity may be elevated here because the crystallized basalts or gabbros (beneath the volcanic seafloor) are more prone to seismogenic rupture than the ultramafic basement (beneath the

smooth seafloor) in which stress may be accommodated by creeps due to serpentinization. Our observations may thus provide a framework to examine earthquake generation at detachment systems, interacting with sparse magmatism.

Maximum depth of earthquakes and the axial thermal regime

The thickness of the axial brittle lithosphere, which is commonly interpreted by the maximum depth of earthquakes[20,25,26], is predicted to increase as spreading rate decreases[20] and/or as melt supply decreases[27]. The 64°30'E region of the ultraslow spreading SWIR, being nearly amagmatic, may be regarded as a calibration for the brittle lithosphere thickness of the MOR system. Although our two OBS deployments only recorded a few hundred microearthquakes, the maximum depth of earthquake hypocenters is on the order of 15 km, and this depth is mostly uniform along the ridge axis, across the transition from volcanic to nearly-avolcanic smooth seafloor (Fig. 2c). The thickness of the brittle lithosphere is mainly controlled by the thermal regime with its base roughly corresponding to the ~650°C isotherm[21,28,29] (i.e., at least 15 km deep at the SWIR 64°30'E). This temperature condition is consistent with the minimum depth of 18 km for the 800-1000°C isotherm at the SWIR 64°30'E, determined from petrological constraints for the high-stress ductile deformation of sheared peridotites[30,31].

A greater maximum depth of microearthquakes (~20 km) was found at the adjacent magma-poor SWIR 65°10'E[32], but these earthquakes were located using a significantly different velocity model constrained from the magmatically-robust segment #8 volcano[33] (Supplementary Fig. 2). We also obtain a maximum earthquake depth of ~20 km if we apply their velocity model to our events (Methods and Supplementary Fig. 8), although this model is absolutely unsuitable to the nearly-amagmatic setting of the SWIR 64°30'E.

Intriguingly, the maximum earthquake depth at the Dragon Horn area (SWIR 49°36'E),

which has the same spreading rate but is more magmatic than the SWIR 64°30'E, is also on the order of 15 km[18,34]. There thus appears to be a disconnection between the maximum earthquake depth and melt supply at ultraslow spreading ridges, putting into question a direct relationship between the thickness of the axial brittle lithosphere and the amount of melt supply to the ridge axis. A recent numerical thermal model provides a possible explanation by considering melt emplacement depth[35]: at a given spreading rate and melt supply, the thermal regime can be colder if melt is emplaced in the shallow hydrothermally-active region. This shallow melt body will be cooled very rapidly, leading to an axial thermal regime beneath the hydrothermal domain that is identical to no melt supply[35].

Microseismicity at detachment systems

The seismicity pattern of the active flip-flop detachment fault at the SWIR 64°30'E is characterized by earthquakes aligned with the trace of the detachment fault plane and by coinciding with antithetic normal faults in the detachment hanging wall (Fig. 3b). The detachment-faulting events are similar to those observed at the more magmatic corrugated detachment faults, such as at 26°10'N[15] (TAG), 13°20'N[16,17], and 14°50’N (Logatchev) of the Mid-Atlantic Ridge[15–17,19] (MAR) and at the SWIR Dragon Horn[18,34]. However, these detachment faults have very few hanging-wall earthquakes (Fig. 3). We propose that the hanging-wall seismicity may be a signature of the nearly-amagmatic flip-flop detachment system, where the plate spreading is accommodated by both detachment and hanging-wall faulting with very few magma intrusions. Such hanging-wall faults may be newly generated as the plate stretches and/or the relic of damage zones of the previous footwall. In contrast to the corrugated mode of detachment faults, magma intrusions are responsible for a considerable part of the plate spreading in the hanging wall, which largely reduces the hanging-wall faulting and seismicity.

In conclusion, our study of two short OBS deployments at the nearly-amagmatic 64°30'E section of the SWIR reveals an active flip-flop detachment fault and its hanging-wall seismicity observed at no other detachment system. We also suggest that the upper limit of lithospheric thickness at oceanic spreading centers may be on the order of 15 km.

Methods

Microearthquake experiments

The first experiment, using 14 OBSs in a cross configuration, recorded 8 days of microearthquakes in between airgun shots during the SISMOSMOOTH active seismic survey in October 2014 (R/V *Marion Dufresne*; SMSMO catalog; Fig. 1). The second experiment, using 6 OBSs in a hexagon configuration, continuously recorded 19 days of microearthquakes during the ROVSMOOTH cruise in December 2016 (R/V *Pourquoi Pas?*; RVSMO catalog; Fig. 1). Each OBS recorded three orthogonal ground motions plus pressure signals, with all channels recording at 250 Hz during the SISMOSMOOTH cruise and at 500 Hz during the ROVSMOOTH cruise.

Earthquake detection

The internal clocks of the OBSs were synchronized on deployment and recovery, and a linear drift correction was applied. Earthquake events were network detected by the CONDET program in the SEISAN software[36] using the STA/LTA trigger algorithm, and an automatic picking procedure[37] was used to pick P and S wave arrival onsets. These events were registered in the SEISAN database, and P- and S-wave arrival onsets were manually refined (Supplementary Fig. 1).

1-D velocity model

The 1-D P-wave velocity model was calculated using the VELEST program[38]. The initial velocity model was extracted from a seismic refraction experiment across DF1 from the

SISMOSMOOTH cruise[23]. This model generally agrees with a broader velocity model at the same area[39] (Supplementary Fig. 2). Only events with OBS ≥6 and GAP≤180° were used in the VELEST program. The best-fitting P-wave velocity model was iteratively searched (Supplementary Fig. 2). The final root-mean-square (RMS) is 107 ms. The S-wave velocity (Vs) model is calculated using a best-fitting Vp/Vs ratio of 1.7, based on the Wadati diagram that plots the travel time of P-wave versus travel time differences of P- and S- waves (S-P time; Supplementary Fig. 3).

Earthquake location and relocation

The initial earthquake locations were searched by the NonLinLoc software with the Oct-tree algorithm[40] and the SWIR 64°30'E velocity model (Supplementary Fig. 2). The maximum likelihood hypocenter is used to locate each earthquake event, and a three-dimension error ellipsoid (68% confidence) is generated from the posterior density function (PDF) scatter samples[40]. 507 events of SMSMO (122) and RVSMO (385) catalogs were located with four or more stations, and 388 events of SMSMO (88) and RVSMO (300) catalogs are well located with horizontal and depth errors of <5 km and RMS residual of <100 ms (Supplementary Figs. 8a-1 to 8d-1). Station corrections, given by the average travel time residuals at each OBS calculated by the NonLinLoc software in an iterative way, were applied for the P and S phases (Supplementary Fig. 4): the mean absolute station correction is 60±40 ms in both catalogs. P- and S-waves travel time residuals follow the Gaussian distribution with an average RMS misfit of 34 ms (Supplementary Fig. 9). Bootstrap analysis of location errors was applied for four chosen groups of NonLinLoc located events to show the stability of the hypocenter estimates: 1) two swarm events in the RVSMO catalog, 2) two deep events in the RVSMO catalog (beneath smooth and volcanic seafloor), 3) one hanging-wall event in the SMSMO catalog, and 4) two detachment-fault events in both SMSMO and RVSMO catalogs (Supplementary Fig. 10).

We also applied the SWIR 65-66°E velocity model[32] (Supplementary Fig. 2), constrained from a more magmatically-robust area than our study area[23,33], to locate earthquakes recorded in our study area using the NonLinLoc software (Supplementary Figs. 8a-2 to 8d-2). Earthquakes with more distant epicenters to the OBS network tend to have deeper hypocenters to form an inverted V shape of along-axis hypocenter depth distribution (Supplementary Figs. 8b-2), which is similar to what was proposed at the SWIR 65-66°E[32].

NonLinLoc hypocenters with six or more stations, horizontal and depth errors of <5 km, and RMS residual of <100 ms, were relocated using the Double-Difference Hypocenter (HypoDD) algorithm[41]. The relocation uses both catalog and cross-correlation (Supplementary Figs. 11a-3 to 11d-3) and runs using the python module HypoDDpy[42]. A time window of 300 ms was applied based on pickings of P and S arrival onsets, and cross-correlated waveforms with a correlation coefficient lower than 0.6 were rejected. Supplementary Fig. 12 shows the differences between the NonLinLoc locations and the HypoDD relocations for 30 randomly selected events. 307 well-constrained absolute hypocenters were relocated with mean relative location errors of 500 m E-W, 400 m N-S, and 500 m in depth.

We also tested catalog only (Supplementary Figs. 11a-1 to 11d-1) and cross-correlation only (Supplementary Figs. 11a-2 to 11d-2) in the HypoDD algorithm, which show more located earthquakes than both catalog and cross-correlation (Supplementary Figs. 11a-3 to 11d-3). Hypocenter location patterns in three algorithms are relatively stable.

Earthquake magnitude calculation

The definition of local magnitudes (M_L) is given by[43]:

$$M_L = log(A) + n\ log(r) + K\ r + C, \quad (1)$$

where A (in nm) is the maximum amplitude of horizontal components picked in the Wood-

Anderson seismogram[44], r (in km) is the hypocentral distance, C is a correction for each OBS, and n and K are constants to be calculated and related to geometrical spreading and attenuation of seismic waves, respectively. The local magnitudes, parameters n and K, and station correction can be solved by a least-squares criterion that produces an optimal solution[45,46]. For the SMSMO and RVSMO catalogs together, we obtain n = -2.923, K = 5.85×10^{-3}, and C = (-3)-(-2). Magnitude completeness (Mc) is determined as 1.1 using the b-value stability approach[47], resulting in a b-value of 0.9.

First-motion focal mechanism

To calculate best-fitting focal mechanisms, we use two first-motion-based algorithms, HASH[48] and FOCMEC[49]. Multiple criteria were applied: apparent first-motion polarities of P-wave onsets ≥8, azimuthal gaps ≤250°, the weighted fraction of misfit polarities <10%, RMS of fault plane uncertainty from HASH ≤35° (95% confidence), and similar reasonable solutions generated by both approaches. Eight acceptable focal mechanisms were found in the SMSMO catalog (Fig. 2). The azimuthal gaps of accepted focal mechanisms are all >90°, so that their quality grades based on the HASH criteria are all in category E (A is the best constrained). We did not obtain focal mechanisms in the RVSMO deployment due to the lesser number of OBSs.

Data availability

OBS locations, two earthquake catalogs, swarm events, and focal mechanisms in this study are provided in the Supplementary Information. Any remaining raw datasets of this study and additional information of the SISMOSMOOTH[50] and ROVSMOOTH[51] cruises are available at https://doi.org/10.17600/14003300 and https://doi.org/10.17600/16002000.

Code availability

The software and codes used in this study included: SEISAN software[36] (http://www.seisan.info/), VELEST program[38] (https://seg.ethz.ch/software/velest.html), NonLinLoc software[40] (http://alomax.free.fr/nlloc/), Double-Difference Hypocenter (HypoDD) algorithm[41] (Version 2.0; https://www.ldeo.columbia.edu/~felixw/hypoDD.html) and its python module HypoDDpy[42] (https://doi.org/10.5281/zenodo.18907), HASH[48] and FOCMEC[49] programs internally in the SEISAN software, and GMT[52] (Version 6; https://www.generic-mapping-tools.org/).

References

1. Cannat, M. *et al.* On spreading modes and magma supply at slow and ultraslow mid-ocean ridges. *Earth Planet. Sci. Lett.* **519**, 223–233 (2019).
2. Sauter, D. *et al.* Continuous exhumation of mantle-derived rocks at the Southwest Indian Ridge for 11 million years. *Nat. Geosci.* **6**, 314–320 (2013).
3. Reston, T. Flipping detachments: The kinematics of ultraslow spreading ridges. *Earth Planet. Sci. Lett.* **503**, 144–157 (2018).
4. Cannat, M. *et al.* Modes of seafloor generation at a melt-poor ultraslow-spreading ridge. *Geology* **34**, 605–608 (2006).
5. Cannat, M. *et al.* A forest of carbonate-brucite chimneys at the Southwest Indian Ridge: the ultramafic-hosted Old City hydrothermal field. in *Goldschmidt Conference Abstract* (2019).
6. Escartín, J. *et al.* Central role of detachment faults in accretion of slow-spreading oceanic lithosphere. *Nature* **455**, 790–794 (2008).
7. Buck, W. R., Lavier, L. L. & Poliakov, A. N. B. Modes of faulting at mid-ocean ridges. *Nature* **434**, 719–723 (2005).
8. Smith, D. K., Escartín, J., Schouten, H. & Cann, J. R. Fault rotation and core complex formation: Significant processes in seafloor formation at slow-spreading mid-ocean ridges (Mid-Atlantic Ridge, 13°-15°N). *Geochemistry, Geophys. Geosystems* **9**, (2008).
9. Olive, J. A. & Dublanchet, P. Controls on the magmatic fraction of extension at mid-ocean ridges. *Earth Planet. Sci. Lett.* **549**, 116541 (2020).
10. Cann, J. R. *et al.* Corrugated slip surfaces formed at ridge-transform intersections on the Mid-Atlantic Ridge. *Nature* **385**, 329–332 (1997).
11. MacLeod, C. J. *et al.* Life cycle of oceanic core complexes. *Earth Planet. Sci. Lett.* **287**, 333–344 (2009).
12. Escartín, J. *et al.* Tectonic structure, evolution, and the nature of oceanic core

complexes and their detachment fault zones (13°20′N and 13°30′N, Mid Atlantic Ridge). *Geochemistry, Geophys. Geosystems* **18**, 1451–1482 (2017).

13. Kong, L. S. L., Solomon, S. C. & Purdy, G. M. Microearthquake characteristics of a mid-ocean ridge along-axis high. *J. Geophys. Res.* **97**, (1992).

14. Tilmann, F., Flueh, E., Planert, L., Reston, T. & Weinrebe, W. Microearthquake seismicity of the Mid-Atlantic Ridge at 5°S: A view of tectonic extension. *J. Geophys. Res. Solid Earth* **109**, (2004).

15. DeMartin, B. J., Sohn, R. A., Pablo Canales, J. & Humphris, S. E. Kinematics and geometry of active detachment faulting beneath the Trans-Atlantic Geotraverse (TAG) hydrothermal field on the Mid-Atlantic Ridge. *Geology* **35**, 711 (2007).

16. Parnell-Turner, R. *et al.* Oceanic detachment faults generate compression in extension. *Geology* **45**, 923–926 (2017).

17. Parnell-Turner, R. *et al.* Seismicity trends and detachment fault structure at 13°N, Mid-Atlantic Ridge. *Geology* **49**, 320–324 (2021).

18. Yu, Z. *et al.* Lithospheric Structure and Tectonic Processes Constrained by Microearthquake Activity at the Central Ultraslow-Spreading Southwest Indian Ridge (49.2° to 50.8°E). *J. Geophys. Res. Solid Earth* **123**, 6247–6262 (2018).

19. Grevemeyer, I., Reston, T. J. & Moeller, S. Microseismicity of the Mid-Atlantic Ridge at 7°S-8°15′S and at the Logatchev Massif oceanic core complex at 14°40′N- 14°50′N. *Geochemistry, Geophys. Geosystems* **14**, 3532–3554 (2013).

20. Phipps Morgan, J. & Chen, Y. J. Dependence of ridge-axis morphology on magma supply and spreading rate. *Nature* **364**, 706–708 (1993).

21. McKenzie, D., Jackson, J. & Priestley, K. Thermal structure of oceanic and continental lithosphere. *Earth Planet. Sci. Lett.* **233**, (2005).

22. Gutenberg, B. & Richter, C. F. Frequency of earthquakes in California. *Bull. Seismol. Soc. Am.* **34**, 185–188 (1944).

23. Momoh, E., Cannat, M., Watremez, L., Leroy, S. & Singh, S. C. Quasi-3-D Seismic Reflection Imaging and Wide-Angle Velocity Structure of Nearly Amagmatic Oceanic Lithosphere at the Ultraslow-Spreading Southwest Indian Ridge. *J. Geophys. Res. Solid Earth* **122**, 9511–9533 (2017).

24. Momoh, E., Cannat, M. & Leroy, S. Internal Structure of the Oceanic Lithosphere at a Melt-Starved Ultraslow-Spreading Mid-Ocean Ridge: Insights From 2-D Seismic Data. *Geochemistry, Geophys. Geosystems* **21**, (2020).

25. Grevemeyer, I. *et al.* Constraining the maximum depth of brittle deformation at slow- and ultraslow-spreading ridges using microseismicity. *Geology* **47**, 1069–1073 (2019).

26. Chen, Y. & Morgan, W. J. A nonlinear rheology model for mid-ocean ridge axis topography. *J. Geophys. Res.* **95**, (1990).

27. Fan, Q., Olive, J. & Cannat, M. Thermo-Mechanical State of Ultraslow-Spreading Ridges With a Transient Magma Supply. *J. Geophys. Res. Solid Earth* **126**, e2020JB020557 (2021).

28. Anderson, D. L. Lithosphere, asthenosphere, and perisphere. *Rev. Geophys.* **33**, 125 (1995).

29. Wang-Pin Chen & Molnar, P. Focal depths of intracontinental and intraplate

earthquakes and their implications for the thermal and mechanical properties of the lithosphere. *J. Geophys. Res.* **88**, (1983).

30. Bickert, M., Cannat, M., Tommasi, A., Jammes, S. & Lavier, L. Strain Localization in the Root of Detachment Faults at a Melt-Starved Mid-Ocean Ridge: A Microstructural Study of Abyssal Peridotites From the Southwest Indian Ridge. *Geochemistry, Geophys. Geosystems* **22**, e2020GC009434 (2021).

31. Bickert, M., Lavier, L. & Cannat, M. How do detachment faults form at ultraslow mid-ocean ridges in a thick axial lithosphere? *Earth Planet. Sci. Lett.* **533**, 116048 (2020).

32. Schlindwein, V. & Schmid, F. Mid-ocean-ridge seismicity reveals extreme types of ocean lithosphere. *Nature* **535**, 276–279 (2016).

33. Minshull, T. A., Muller, M. R. & White, R. S. Crustal structure of the Southwest Indian Ridge at 66°E: Seismic constraints. *Geophys. J. Int.* **166**, 135–147 (2006).

34. Tao, C. *et al.* Deep high-temperature hydrothermal circulation in a detachment faulting system on the ultra-slow spreading ridge. *Nat. Commun.* **11**, 1–9 (2020).

35. Chen, J., Olive, J. A. & Cannat, M. Thermal Regime of Slow and Ultraslow Spreading Ridges Controlled by Melt Supply and Modes of Emplacement. *J. Geophys. Res. Solid Earth* **127**, e2021JB023715 (2022).

36. Havskov, J. & Ottemöller, L. SeisAn earthquake analysis software. *Seismol. Res. Lett.* **70**, 532–534 (1999).

37. Baillard, C., Crawford, W. C., Ballu, V., Hibert, C. & Mangeney, A. An automatic kurtosis-based P-and S-phase picker designed for local seismic networks. *Bull. Seismol. Soc. Am.* **104**, 394–409 (2014).

38. Kissling, E., Ellsworth, W. L., Eberhart-Phillips, D. & Kradolfer, U. Initial reference models in local earthquake tomography. *J. Geophys. Res.* **99**, 19635–19646 (1994).

39. Corbalán, A. *et al.* Seismic Velocity Structure Along and Across the Ultraslow-Spreading Southwest Indian Ridge at 64°30′E Showcases Flipping Detachment Faults. *J. Geophys. Res. Solid Earth* **126**, e2021JB022177 (2021).

40. Lomax, A., Virieux, J., Volant, P. & Berge-Thierry, C. Probabilistic Earthquake Location in 3D and Layered Models. in *Modern Approaches in Geophysics* 101–134 (Springer, Dordrecht, 2000). doi:10.1007/978-94-015-9536-0_5.

41. Waldhauser, F. & Ellsworth, W. L. A Double-difference Earthquake location algorithm: Method and application to the Northern Hayward Fault, California. *Bull. Seismol. Soc. Am.* **90**, 1353–1368 (2000).

42. Krischer, L. hypoDDpy: hypoDDpy 1.0. (2015) doi:10.5281/ZENODO.18907.

43. Richter, C. F. An instrumental earthquake magnitude scale*. *Bull. Seismol. Soc. Am.* **25**, 1–32 (1935).

44. Anderson, J. A. & Wood, H. O. Description and theory of the torsion seismometer. *Bull. Seismol. Soc. Am.* **15**, 1–72 (1925).

45. Illsley-Kemp, F. *et al.* Local earthquake magnitude scale and b-value for the Danakil region of northern afar. *Bull. Seismol. Soc. Am.* **107**, (2017).

46. Keir, D., Stuart, G. W., Jackson, A. & Ayele, A. Local earthquake magnitude scale and seismicity rate for the Ethiopian rift. *Bull. Seismol. Soc. Am.* **96**, (2006).

47. Cao, A. & Gao, S. S. Temporal variation of seismic b-values beneath northeastern Japan island arc. *Geophys. Res. Lett.* **29**, (2002).

48. Hardebeck, J. L. & Shearer, P. M. A new method for determining first-motion focal mechanisms. *Bull. Seismol. Soc. Am.* **92**, (2002).

49. Snoke, J., Munsey, J., Teague, A. & Bollinger, G. A program for focal mechanism determination by combined use of polarity and SV-P amplitude ratio data. *Earthq. notes* **55**, 15 (1984).

50. Leroy, S. & Cannat, M. MD 199 / SISMO-SMOOTH cruise,. *RV Marion Dufresne* (2014) doi:10.17600/14003300.

51. Cannat, M. ROVSMOOTH cruise. *RV Pourquoi pas ?* (2016) doi:10.17600/16002000.

52. Wessel, P. *et al.* The Generic Mapping Tools Version 6. *Geochemistry, Geophys. Geosystems* **20**, (2019).

53. Simão, N. M. *et al.* 3-D P-wave velocity structure of oceanic core complexes at 13°N on the Mid-Atlantic Ridge. *Geophys. J. Int.* **221**, 1555–1579 (2020).

54. Zhao, M., Canales, J. P. & Sohn, R. A. Three-dimensional seismic structure of a Mid-Atlantic Ridge segment characterized by active detachment faulting (Trans-Atlantic Geotraverse, 25°55′N-26°20′N). *Geochemistry, Geophys. Geosystems* **13**, 2012GC004454 (2012).

Acknowledgments

We thank Sylvie Leroy, chief scientist of the SISMOSMOOTH cruise, the science parties, and the crews of the RVs *Marion Dufresne* and *Pourquoi Pas?* for collecting the data. We also thank Zhiteng Yu, Soumya Bohidar, and Aude Lavayssière for their help in the data processing. All figures were created using the GMT software[52]. We thank the funding of the ANR project "Ridge-Factory-Slow" (ANR-18-CE010002-01). Jie Chen was supported by the China Scholarship Council (201808330437). This is IPGP contribution #4239.

Author Contributions Statement

J.C. processed the microseismicity data and wrote the manuscript. W.C. supervised data processing, interpretation, and writing. M.C. developed the project, participated in the SISMOSMOOTH and ROVSMOOTH cruises, led the data collection, and supervised interpretation and writing.

365 **Competing Interests Statement**

366 The authors declare no competing interests.

367

368 **Fig. 1 | OBS locations and tectonic interpretation of the flip-flop detachment fault**
369 **system at the eastern SWIR.** (a) Tectonic map with locations of the OBS networks:
370 SMSMO (14 OBSs) and RVSMO (6 OBSs). The base map is created based on shipborne
371 bathymetry data[4]. Geological and tectonic information (see legend for symbols) includes
372 breakaways (B1-B6) and emergences (E1-E6) of successive detachment faults, corrugated
373 surface, the boundary between volcanic and smooth seafloor, and linear sketches of scarps
374 and volcanic ridges[1]. Yellow star is the low-temperature Old City hydrothermal field with
375 carbonate-brucite chimneys[5]. The white dashed square marks the bounds of Fig. 2a. (b)
376 Tectonic interpretation of the successive flip-flop detachment fault system along the PP'
377 cross-section1. Black and gray dashed lines are the 7.5 km/s velocity contours[23,39]. Locations
378 of OBSs are projected to the PP' cross-section. bsl: below sea level.

379

380 **Fig. 2 | Distribution of earthquakes and focal mechanisms.** (**a**) Bathymetric map of the
381 SWIR 64°30'E area showing 307 events of the SMSMO (blue circles) and RVSMO (orange
382 circles) catalogs, the RVSMO seismic swarm (green circles), and 8 determined focal
383 mechanisms. Cross in the legend shows the average absolute horizontal location uncertainty
384 of 3.2 km (1σ). Geological information (see legend for symbols) includes breakaways,
385 emergences, and the boundary between volcanic and smooth seafloor[1]. Best-fitting focal
386 mechanisms have clear upward (black dots) and downward (white dots) first motions of P-
387 wave onsets (Methods). Depth profiles (P0-P0' to P3-P3') are marked as labelled white lines
388 in Fig 2a, with white dashed squares showing the corresponding boundaries for projected
389 earthquakes in Figs. 2c-2f. (**b**) Histograms of earthquake depths below seafloor for the
390 SMSMO (blue) and RVSMO (orange) catalogs, including the seismic swarm (green). (**c**)
391 Along-axis depth profile P0-P0' projecting earthquakes within ±8 km off the profile (VE=1
392 and the same below). Vertical bar shows the average absolute vertical uncertainty of 2.8 km
393 (1σ). The classification of volcanic (pink) and smooth (green) seafloor is indicated[4]. Gray
394 dashed line is the 7.5 km/s velocity contour[39]. Labelled gray dashed lines show depths below
395 the seafloor (the same below). (**d**) and (**e**) Across-axis depth profiles P1-P1' and P2-P2'

projecting earthquakes within ±3 km off the profiles. Black dashed lines indicate the fault plane adapted from Fig. 2f. (**f**) Across-axis depth profile P3-P3' projecting earthquakes within ±5 km off the profile. Dotted lines represent seismic reflectors, interpreted as DF1 damage zone[23], with the main detachment fault plane tentatively drawn in the center (subseafloor solid black line). Black[23] and gray[39] dashed lines are the 7.5 km/s velocity contours. Focal mechanisms are projected to profiles P2-P2' and P3-P3'.

Fig. 3 | Modes of detachment faults and their patterns of seismicity. (**a**) 2D conceptual sketches of amagmatic flip-flop and magmatic corrugated modes of detachment faults. The flip-flop mode may have more hanging-wall faults to accommodate part of the plate spreading, while this part of plate spreading at the corrugated mode is accommodated by magma intrusions. (**b-d**) Microseismicity at the SWIR 64°30'E (this study), and the MAR 26°10'N[15] and 13°20'N[16,17] (VE=1). Labelled dashed black lines show velocity contours of 7.5 km/s (SWIR 64°30'E[39] and MAR 13°20'N[53]) and 7 km/s (MAR 26°10'N[54]). Yellow star is the low-temperature Old City hydrothermal vent. Red stars are high-temperature hydrothermal vents. NVR: neovolcanic ridge. B: breakaway. E: emergence.

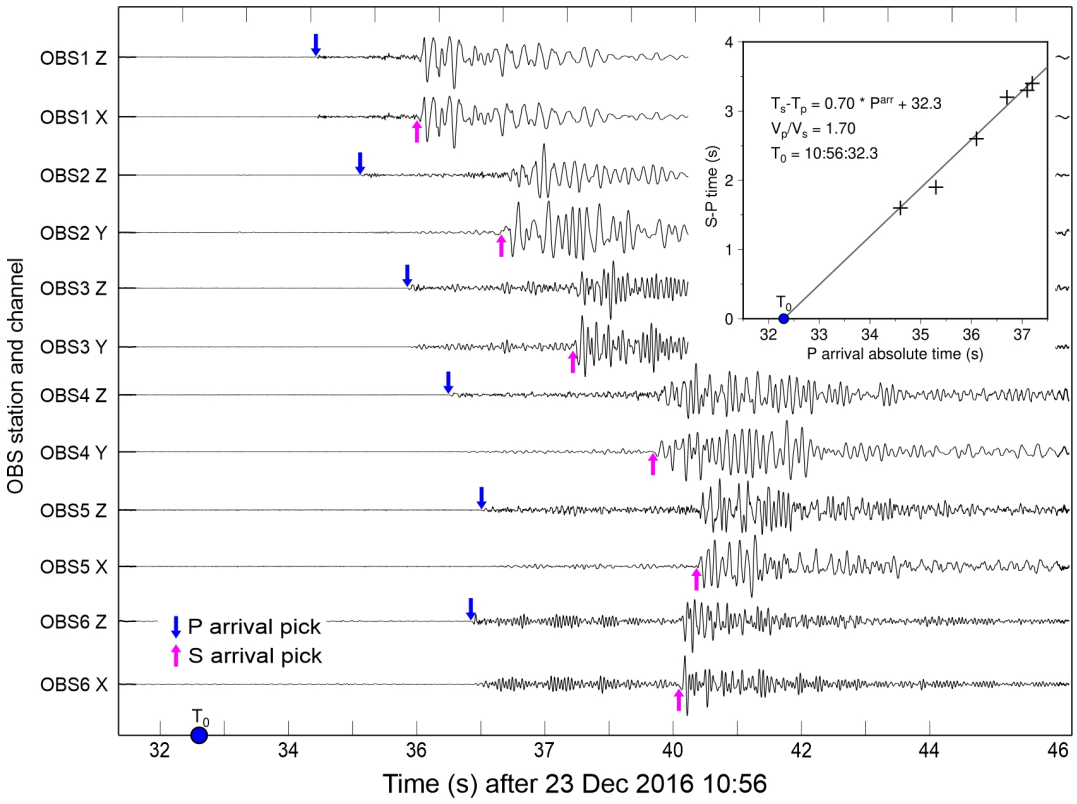

414

415 **Supplementary Fig. 1 | Typical event waveforms.** The event occurred at
416 64.394°E/27.883°S 11.7 km below seafloor with a local magnitude of 2.3, at 10:56, 23 Dec
417 2016 in RVSMO catalog. The inset shows the P-wave arrival absolute time versus arrival
418 time differences of P- and S-waves (S-P time), yielding the origin time (T0) of 10:56:32.3
419 and a Vp/Vs ratio of 1.7.

420

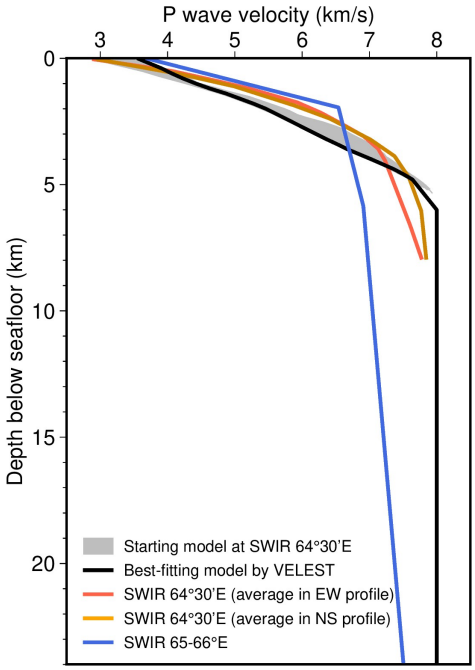

421

422 **Supplementary Fig. 2 | 1-D P wave velocity model.** Starting model (gray area) at the SWIR
423 64°30'E is extracted from a seismic refraction experiment[23]. The best-fitting model (black
424 line) is iteratively searched by the VELEST program[38]. Red and orange lines are average
425 velocity models in EW and NS profiles at the SWIR 64°30'E[39]. Blue line is the velocity
426 model at the SWIR 65-66°E[32].

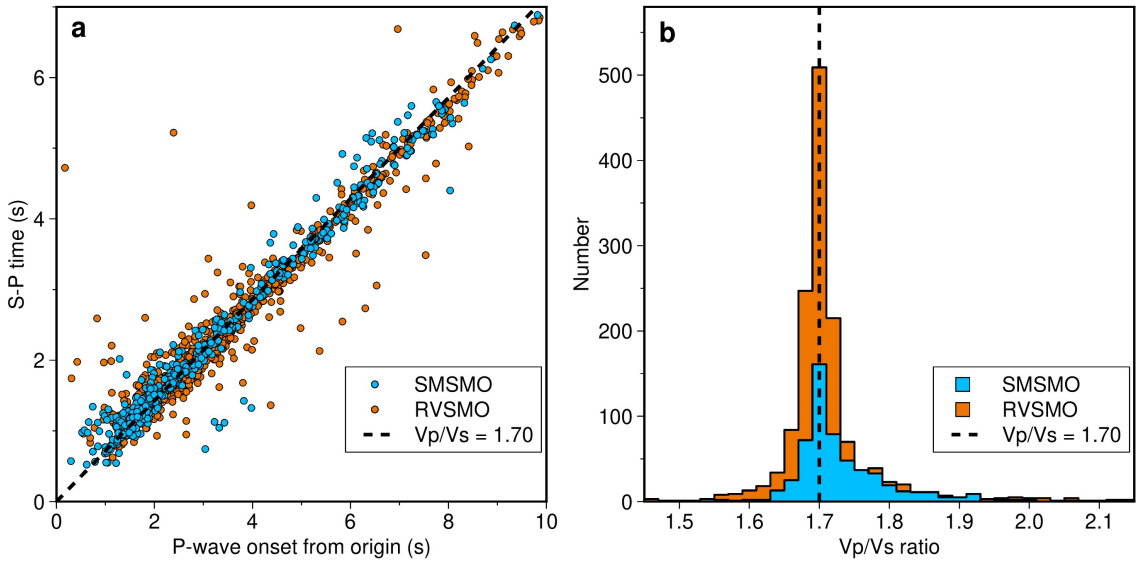

427

428 **Supplementary Fig. 3 | Wadati diagram**. (**a**) P-wave onset from origin versus S-P time
429 (Wadati diagram) for both SMSMO (orange) and RVSMO (blue) catalogs. (**b**) Histogram of
430 Vp/Vs ratio Vp/Vs ratio is calculated from the slopes of the Wadati diagram. The best-fitting
431 Vp/Vs ratio is 1.7.

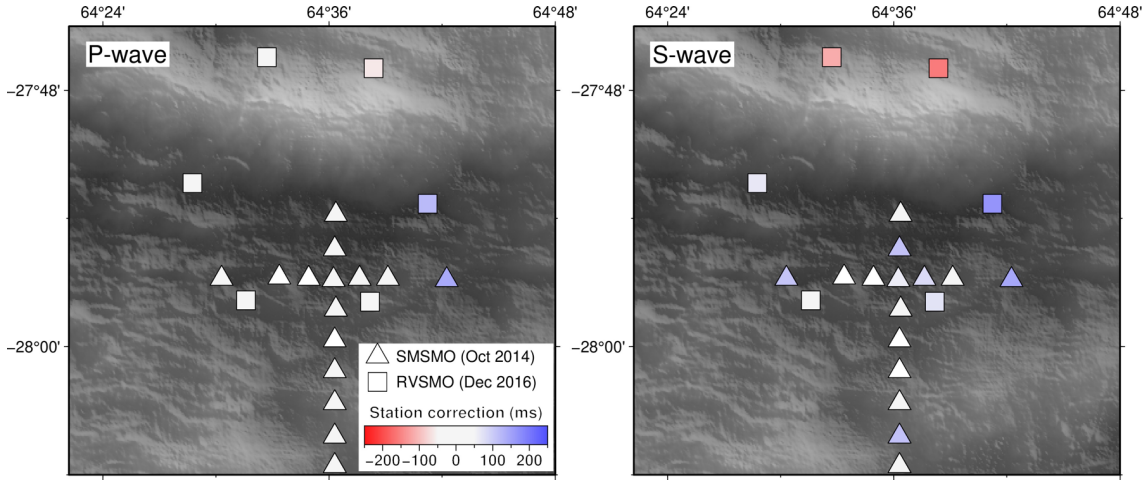

Supplementary Fig. 4 | Station corrections of P- and S-wave returned by NonLinLoc.

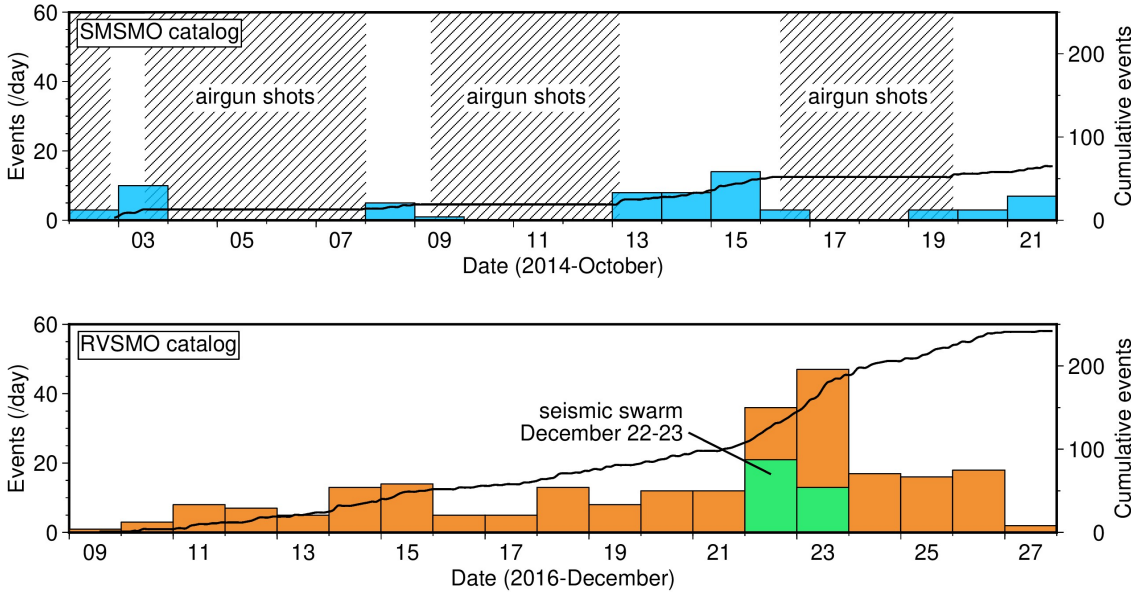

Supplementary Fig. 5 | Histogram and cumulative histogram of located earthquakes for the SMSMO and RVSMO catalogs.

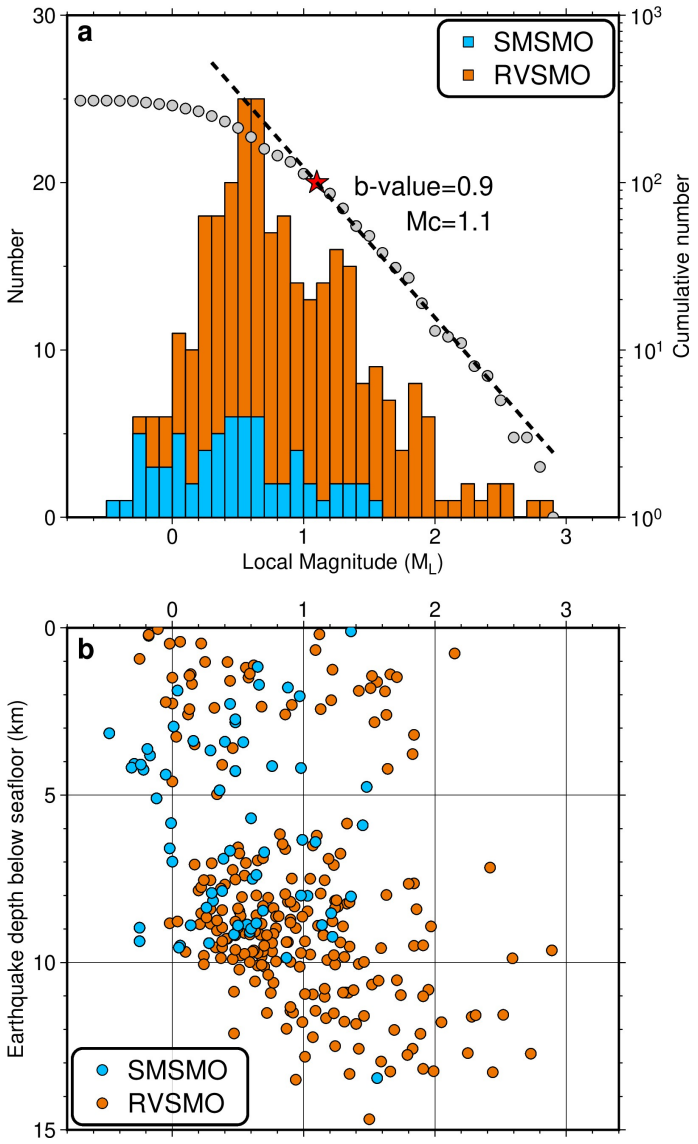

438

439 **Supplementary Fig. 6 | Distribution of local magnitude (M_L).** (**a**) Histograms of local
440 magnitude for the SMSMO (blue) and RVSMO (orange) catalogs (left Y-axis). The
441 cumulative number of earthquakes for both catalogs (gray circles) as a function of local
442 magnitude (right Y-axis). Magnitude completeness (Mc) is determined as 1.1 (red star) using
443 the b-value stability approach[47], resulting in a b-value of 0.9 (slope of the dashed line). (**b**)
444 Local magnitude as a function of earthquake depth for the SMSMO (blue) and RVSMO
445 (orange) catalogs.

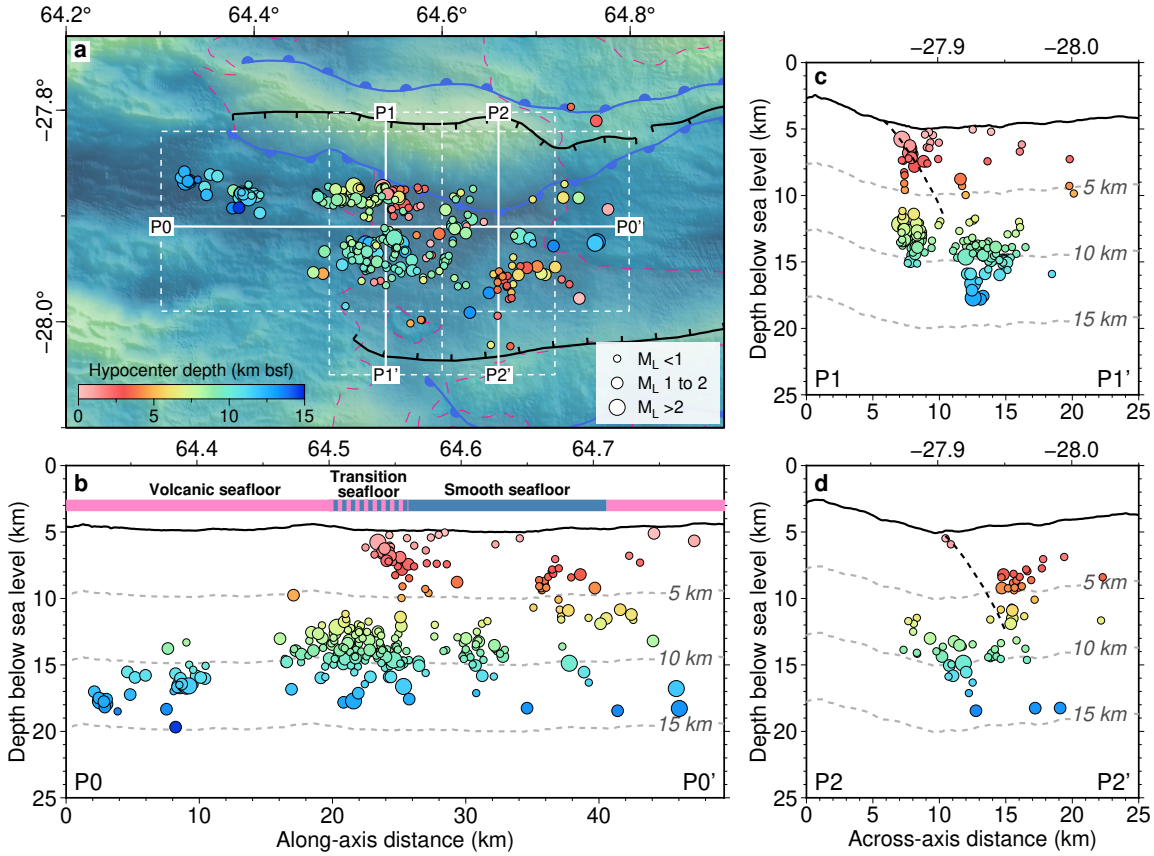

446

447 **Supplementary Fig. 7 | Earthquake relocations, color coded based on hypocenter depths**

448 **and circle size based on local magnitude (M_L).**

449

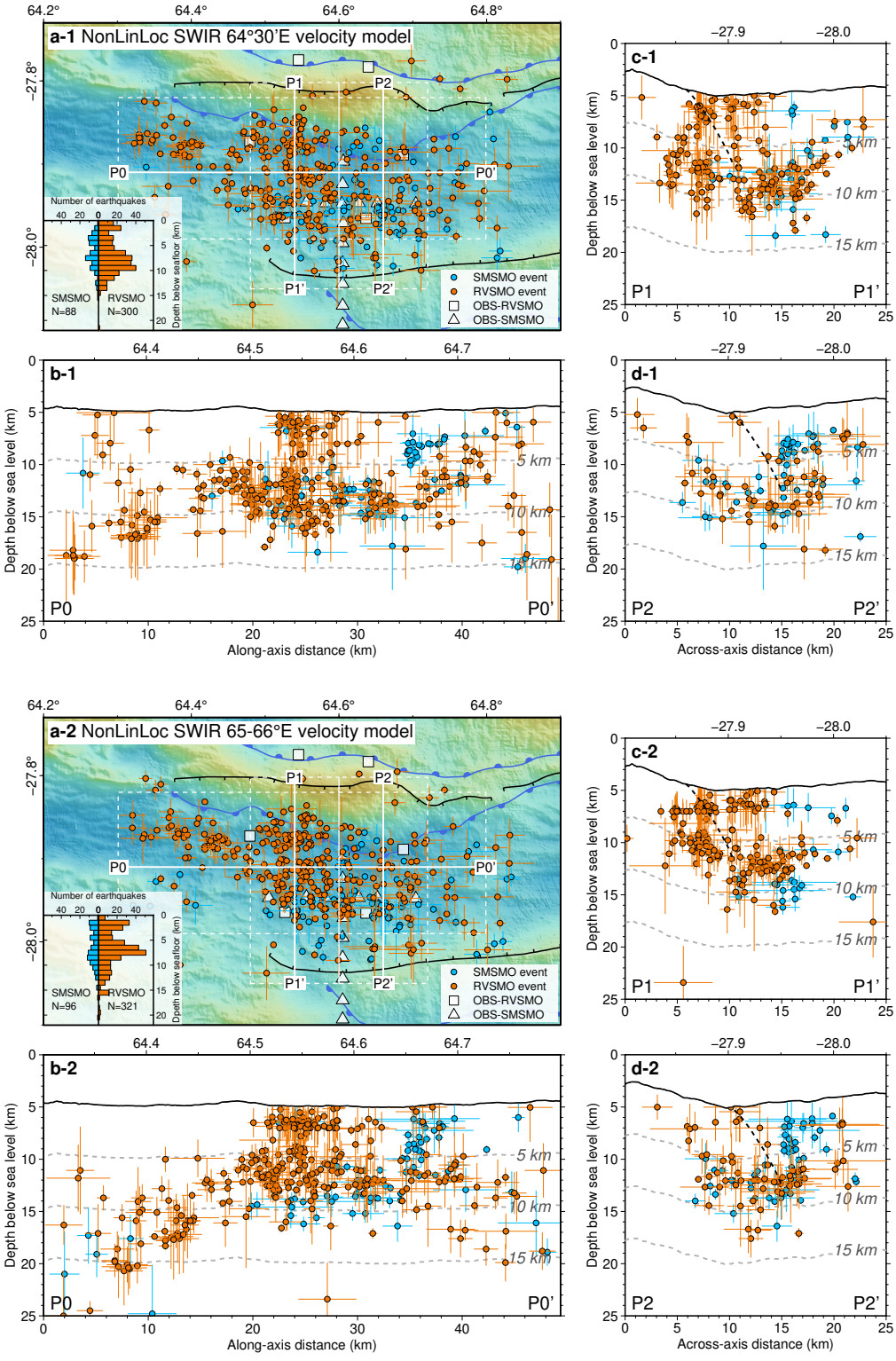

Supplementary Fig. 8 | Earthquake locations. See legend for symbols. Earthquake locations using the NonLinLoc with the SWIR 64°30'E velocity model (**a-1** to **d-1**). Earthquake locations using the NonLinLoc with the SWIR 65-66°E velocity model (**a-2** to **d-2**), compared with the NonLinLoc results with the SWIR 64°30'E velocity model (pale gray). Velocity models see Supplementary Fig. 2. Error bars represent absolute location errors.

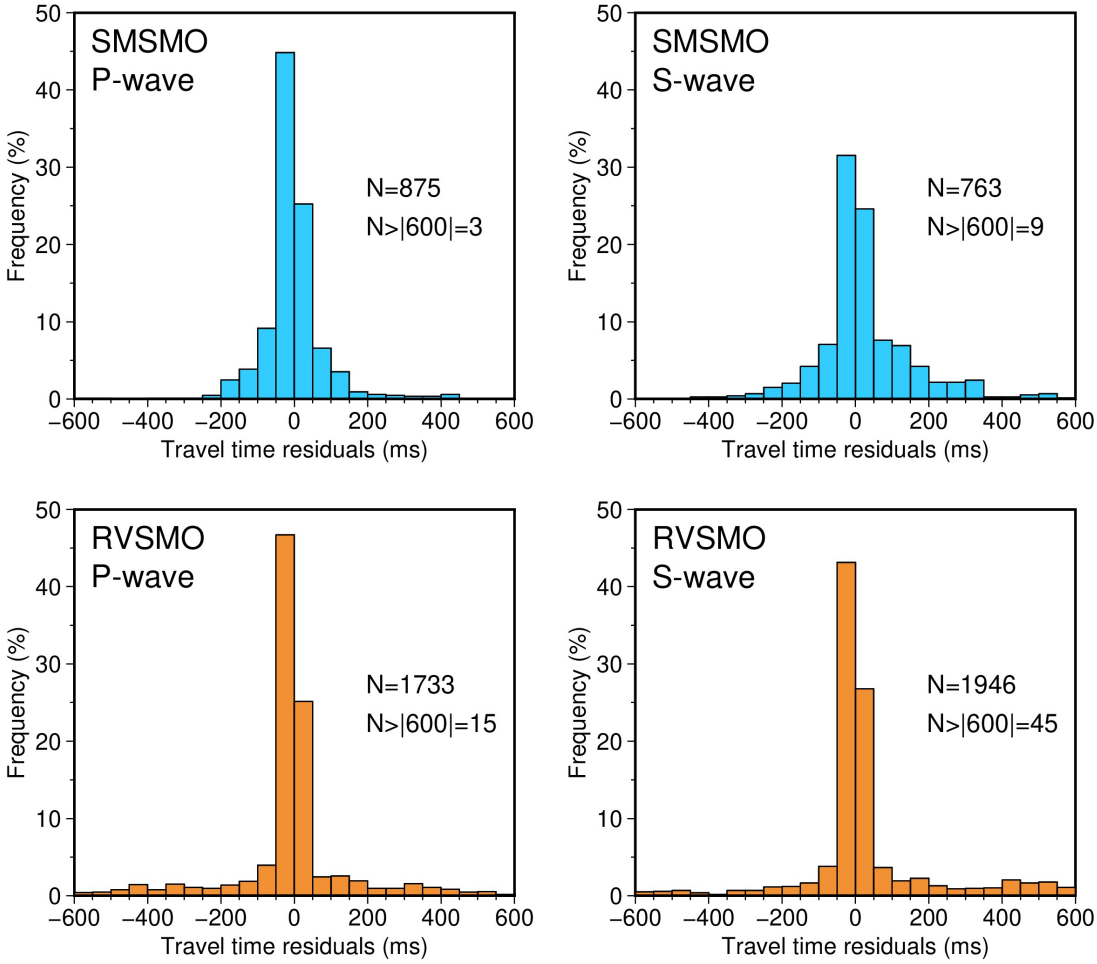

456

457 **Supplementary Fig. 9 | Frequency distribution of P- and S-wave travel time residuals**
458 **for the SMSMO (blue) and RVSMO (orange) catalogs.**

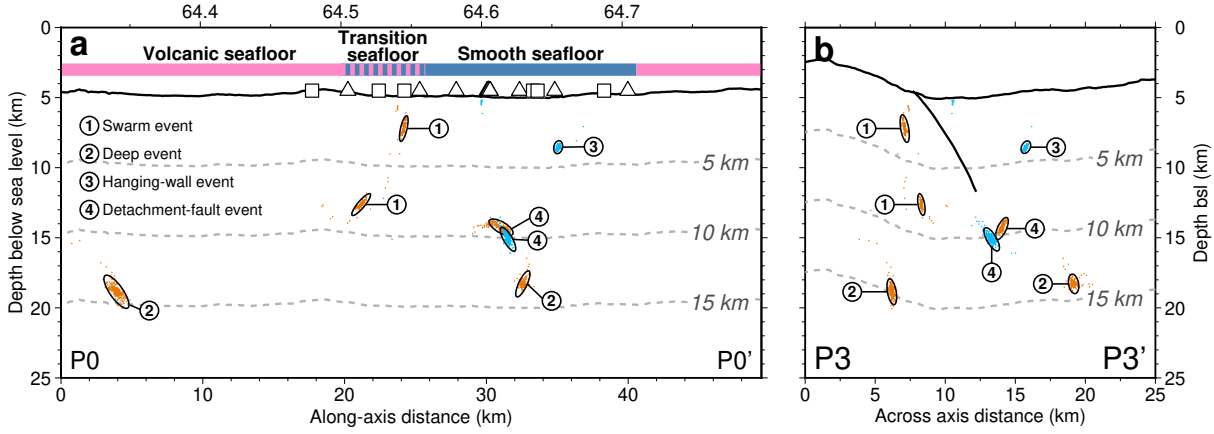

459

460 **Supplementary Fig. 10 | Bootstrap analysis of location errors for four chosen groups of**
461 **NonLinLoc located events.** Blue and orange dots represent events in the SMSMO and
462 RVSMO catalogs, respectively. Perturbations were randomly applied 300 times to P and S
463 arrivals, which were constrained by travel time residuals shown in Supplementary Fig. 9.

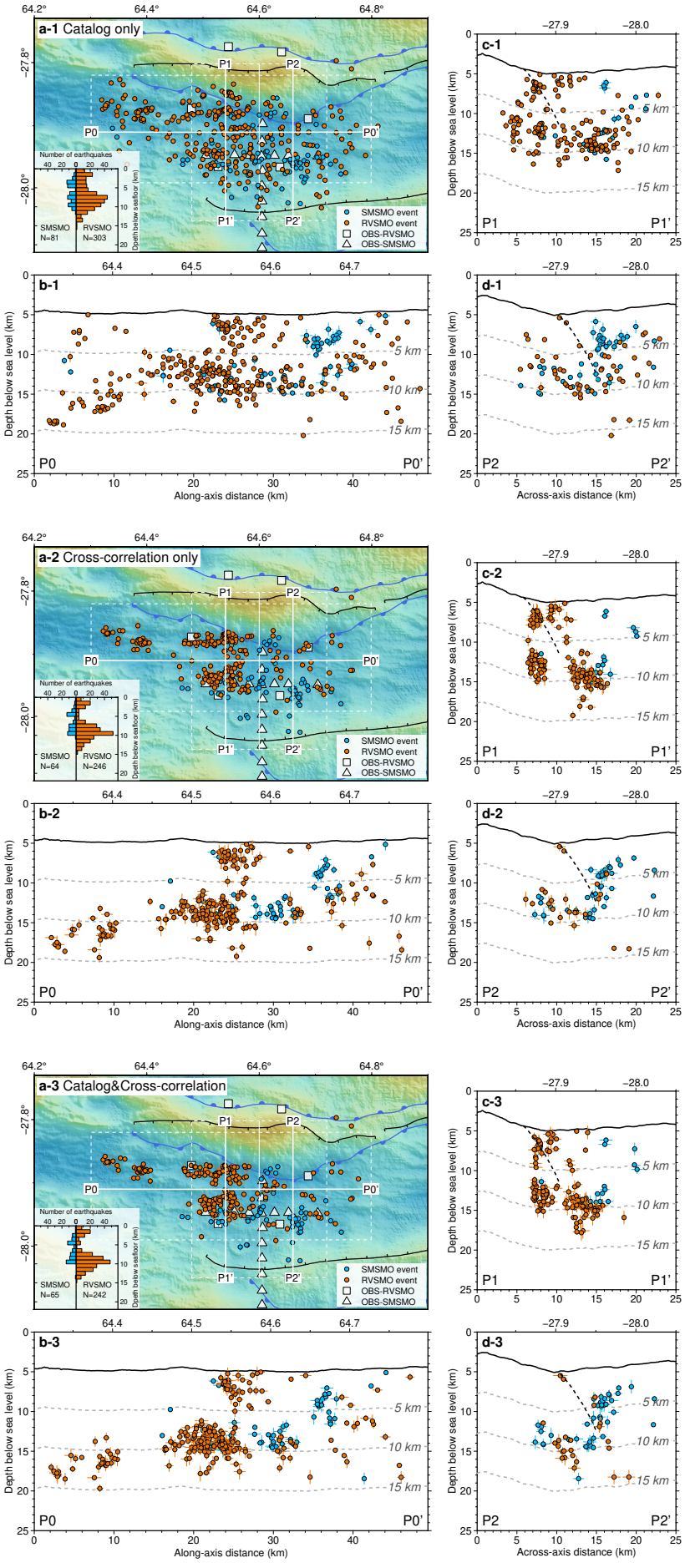
a-1 Catalog only
a-2 Cross-correlation only
a-3 Catalog&Cross-correlation
b-1
b-2
b-3
c-1
c-2
c-3
d-1
d-2
d-3
P0
P0'
P1
P1'
P2
P2'
SMSMO event
RVSMO event
OBS-RVSMO
OBS-SMSMO
Number of earthquakes
Depth below seafloor (km)
SMSMO N=81
RVSMO N=303
SMSMO N=64
RVSMO N=246
SMSMO N=65
RVSMO N=242
5 km
10 km
15 km
Depth below sea level (km)
Along-axis distance (km)
Across-axis distance (km)

Supplementary Fig. 11 | Earthquake relocations. See legend for symbols. Tests of earthquake relocation using the HypoDD with catalog only (**a-1** to **d-1**), cross-correlation only (**a-2** to **d-2**), and catalog&cross-correlation (**a-3** to **d-3**; same results as Fig. 2). Error bars represent relative location errors.

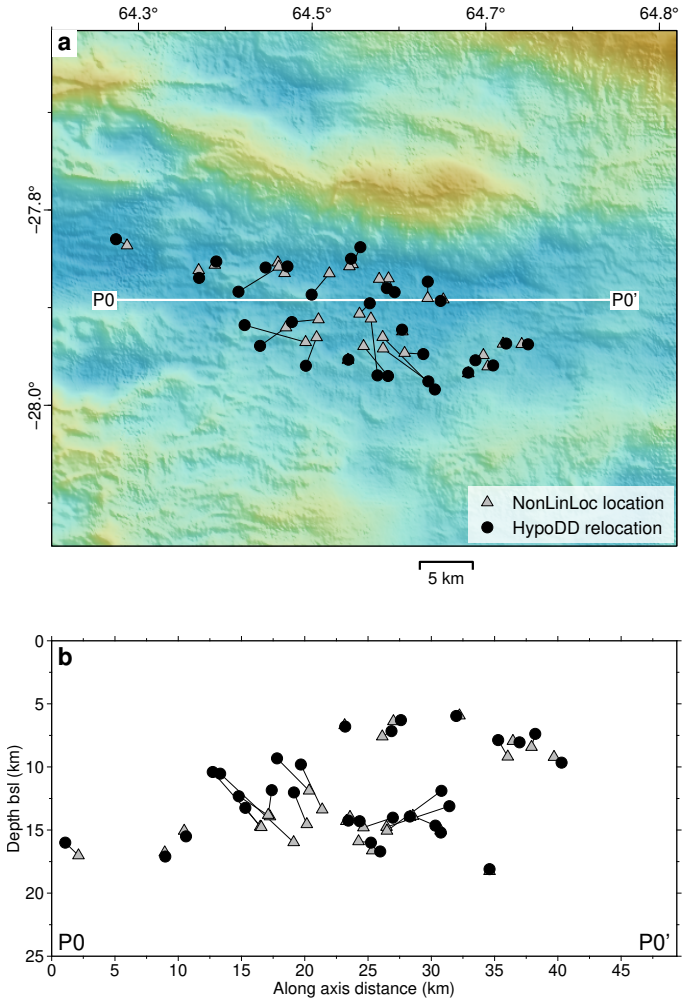

Supplementary Fig. 12 | Differences of NonLinLoc locations and HypoDD relocations for 30 randomly selected events. Each event is connected by a black line between the results of the NonLinLoc location and the HypoDD relocation (catalog&cross-correlation). (**a**) Map view. (**b**) events projected on the along-axis P0-P0' profile.

Inventory of Supporting Information

Supplementary Figs. 1-12.

FocalMechanism.txt

OBS_station.txt

RVSMO_catalog.txt

SMSMO_catalog.txt

Swarm_Dec22_23_2016.txt